

A novel $(\text{La}_{0.2}\text{Ce}_{0.2}\text{Gd}_{0.2}\text{Er}_{0.2}\text{Tm}_{0.2})_2(\text{WO}_4)_3$ high-entropy ceramic material for thermal neutron and gamma-ray shielding

Xuesong Zhang^{a,c,d,e,f}, Yuguang Li^b, Changxiang Li^b, Fan Yang^{a,c,d,e,*}, Zhengming Jiang^{a,c,d,e,*}, Liyan Xue^{a,c,d,e}, Zhiheng Shao^{a,c,d,e}, Zhigang Zhao^{a,c,d,e}, Meiyang Xie^{a,c,d,e}, Shuwen Yu^{a,c,d,e}

^a Fujian Province Joint Innovation Key Laboratory of Fuel and Materials in Clean Nuclear Energy System, Fujian Institute of Research on the Structure of Matter, Chinese Academy of Sciences, Fuzhou 350002, China

^b Science and Technology on Reactor System Design Technology Laboratory, Nuclear Power Institute of China, Chengdu 610213, China

^c Ganjiang Innovation Academy, Chinese Academy of Sciences, Jiangxi Institute of Rare Earths, Chinese Academy of Sciences, Ganzhou 341000, China

^d CAS Key Laboratory of Design and Assembly of Functional Nanostructures, and Fujian Provincial Key Laboratory of Nanomaterials, Fujian Institute of Research on the Structure of Matter, Chinese Academy of Sciences, Fuzhou 350002, China

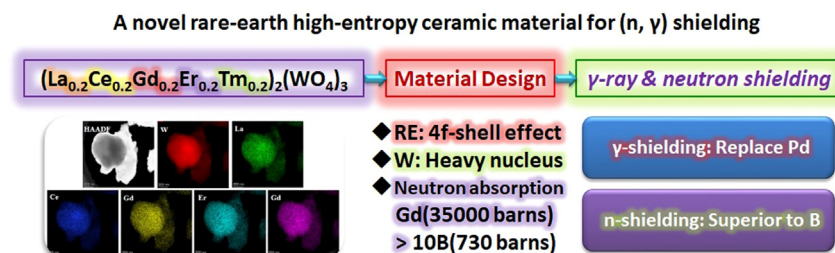
^e Xiamen Key Laboratory of Rare Earth Photoelectric Functional Materials, Xiamen Institute of Rare Earth Materials, Haixi Institute, Chinese Academy of Sciences, Xiamen 361021, China

^f College of Chemical Engineering, Fuzhou University, Fuzhou 350002, China

HIGHLIGHTS

- $(\text{La}_{0.2}\text{Ce}_{0.2}\text{Gd}_{0.2}\text{Er}_{0.2}\text{Tm}_{0.2})_2(\text{WO}_4)_3$ ceramic was prepared by solid-phase synthesis.
- $(\text{La}_{0.2}\text{Ce}_{0.2}\text{Gd}_{0.2}\text{Er}_{0.2}\text{Tm}_{0.2})_2(\text{WO}_4)_3$ /epoxy resin blocks more than 99% of neutrons.
- The lead equivalent of EP/W3 exceeds 0.43 mmPb at 65 keV.
- The composite materials have completed standard testing.

GRAPHICAL ABSTRACT



ARTICLE INFO

Article history:

Received 4 December 2020

Revised 6 April 2021

Accepted 7 April 2021

Available online 9 April 2021

Keywords:

Rare earth

High-entropy ceramic

Solid-phase synthesis

Epoxy resin

Radiation shielding

ABSTRACT

In this study, a new type of $(\text{La}_{0.2}\text{Ce}_{0.2}\text{Gd}_{0.2}\text{Er}_{0.2}\text{Tm}_{0.2})_2(\text{WO}_4)_3$ single-phase high-entropy ceramic (HEC) powder was designed, prepared by solid-phase synthesis, and evenly mixed into an epoxy resin (EP) matrix to test the thermal neutron and γ -ray shielding performance. In terms of γ -ray shielding, $(\text{La}_{0.2}\text{Ce}_{0.2}\text{Gd}_{0.2}\text{Er}_{0.2}\text{Tm}_{0.2})_2(\text{WO}_4)_3$ showed a higher lead equivalent value than EP at 65 keV, indicating a clear shielding effect in the feeble absorbing area of lead-based and bismuth-based materials; moreover, $(\text{La}_{0.2}\text{Ce}_{0.2}\text{Gd}_{0.2}\text{Er}_{0.2}\text{Tm}_{0.2})_2(\text{WO}_4)_3$ showed good γ -ray shielding performance in both low-energy and medium-energy regions. In terms of thermal neutron shielding, the composite with the highest HEC content (EP/W3) had a nearly 100% shielding efficiency, while that of EP was approximately 50%, indicating that this material has favorable thermal neutron and γ -ray shielding performance. Moreover, the thermal conductivity of the resulting composite material was lower than $0.3 \text{ W} \cdot \text{m}^{-1} \cdot \text{K}^{-1}$, the tensile strength was higher than 10 MPa, and the density was lower than $1.5 \text{ g} \cdot \text{cm}^{-3}$. All these results suggest that $(\text{La}_{0.2}\text{Ce}_{0.2}\text{Gd}_{0.2}\text{Er}_{0.2}\text{Tm}_{0.2})_2(\text{WO}_4)_3$ is a candidate radiation shielding material.

© 2021 The Authors. Published by Elsevier Ltd. This is an open access article under the CC BY-NC-ND license (<http://creativecommons.org/licenses/by-nc-nd/4.0/>).

* Corresponding authors at: Xiamen Institute of Rare Earth Materials, Haixi Institute, Chinese Academy of Sciences, Xiamen 361021, China.

E-mail addresses: fanyang2013@fjirsm.ac.cn (F. Yang), xmjiangzhengming@fjirsm.ac.cn (Z. Jiang).

1. Introduction

With the rapid development of science and technology, nuclear energy—a clean energy source—is being developed by countries worldwide. The application of nuclear energy is becoming increas-

ingly common in human life [1–3], ranging from the continuous construction of nuclear power plants to research on small nuclear batteries. However, these applications can inflict constant damage on the human body and the natural environment. Therefore, the demand for new materials with outstanding radiation shielding properties has become increasingly urgent. Traditionally, the most commonly used γ -ray shielding materials are lead [4–8] and concrete [9–11], but these two materials have some drawbacks, including excessive density and weight; furthermore, lead is highly toxic and has poor performance in shielding γ -rays with energy ranging from 40 to 88 keV, termed the “lead feeble absorbing area”, which is not conducive to its future commercialization. In recent years, bismuth tungstate has been extensively studied as a substitute for lead-based materials. Unfortunately, like lead-based materials, bismuth tungstate has a feeble absorbing area between 36.4 keV and 90.5 keV [12], and Bi will decay into Po-210, which is radioactive, after being irradiated by neutrons. Therefore, countries around the worldwide are actively developing new lead-free radiation shielding materials to protect human health. Organics with moderate to high Z levels are becoming candidates for shielding materials due to their mechanical properties, chemical stability, and bonding strength, and epoxy resin-coated ceramic powder with shielding performance is becoming a representative of this type of material [1,13–18]. Currently, radiation shielding materials embedded in polymers include tungsten [17,19], boron [16,20,21], zirconium [22], bismuth [19,23,24], and gadolinium [25–27].

Recently, high-entropy ceramics (HECs), which have evolved through the development of high-entropy alloys (HEAs), have become popular because of their special elemental composition and their many properties that are superior to those of traditional ceramics [28–30]. Since Rost and Curtarolo et al. first reported an entropy-stabilized ceramic with a rock salt structure in 2015 [31], research on HECs has been extended to include oxide ceramics, such as fluorite [32–34], perovskite [35–37], spinel [38], and pyrochlore (or defective fluorite) [39,40], and high-entropy nonoxide ceramics, such as borides [41–43], carbides [44–46], nitrides [47] and silicides [48]. Recently, a team from the University of Nebraska-Lincoln applied high-entropy carbide ceramics to the field of radiation damage. The team used spark plasma sintering (SPS) to synthesize $(\text{Zr}_{0.25}\text{Ta}_{0.25}\text{Nb}_{0.25}\text{Ti}_{0.25})\text{C}$ with a single-phase rock salt structure [49]. The samples were irradiated with Zr ions at different temperatures, and the results showed that there was almost no phase change after irradiation, no pores or segregation formed, and the hardness increased, indicating that the materials have high radiation resistance and physical properties.

In actual applications, neutron and γ radiation usually occur simultaneously, so developing a material that absorbs neutrons and shields γ -rays at the same time is crucial. Rare earth elements meet the requirements; on the one hand, rare earth elements have a relatively high neutron capture cross section, which can effectively absorb neutrons, and on the other hand, rare earth elements are considered to be candidates for compensating for the lead feeble absorbing area and reducing the risk of lead poisoning to organisms [50–53]. In addition, tungsten is already widely used in radiation shielding materials [54,55]. But unfortunately, most elemental metals, especially rare earth metals, are prone to oxidation and failure under natural conditions, which is extremely disadvantageous. Based on the above reasons, in this study, a novel type of $(\text{La}_{0.2}\text{Ce}_{0.2}\text{Gd}_{0.2}\text{Er}_{0.2}\text{Tm}_{0.2})_2(\text{WO}_4)_3$ rare earth tungstate-based HEC powder was successfully designed and prepared by high-temperature solid-phase synthesis. The phase stability brought about by the high entropy effect will make the powder less prone to failure when exposed to radiation, and the selection of

lead-free elements solves the problem of environmental pollution and harm to human health caused by lead-based materials. The k-edge of rare earth elements selected in this system covers the entire lead feeble absorbing area, and Gd has a large neutron capture cross section. Moreover, because γ -ray shielding requires samples with a diameter of 20 cm, the powder was uniformly dispersed in an epoxy matrix at different mass fractions to characterize the shielding performance of the powder. In order to exclude the influence of the matrix material, the blank sample was also tested. The experimental results showed that the high-entropy ceramic powder designed in this work has favorable thermal neutron and γ -ray shielding properties, and the resulting composite material has certain practical mechanical properties.

2. Experimental methods

2.1. Materials

All purchased reagents were used as received without further purification. La_2O_3 (99.99%), CeO_2 (99.99%), Gd_2O_3 (99.99%), and Er_2O_3 (99.99%) were purchased from Fujian Changting Jinlong Rare Earth Co. Ltd., Longyan, China. Tm_2O_3 (99.99%) was purchased from Aladdin Biochemical Technology Co. Ltd., Shanghai, China. WO_3 (99.99%, 50 nm) was purchased from Xiamen Ostor Technology Co. Ltd., Xiamen, China. Polyamide curing agent (651; amine value: 380–420 mg KOH/g; viscosity: 2000–7000 MPa·s), epoxy resin (E-51) and n-butanol (AR, 99%) were purchased from Shanghai Macklin Biochemical Co. Ltd., Shanghai, China.

2.2. Preparation of the $(\text{La}_{0.2}\text{Ce}_{0.2}\text{Gd}_{0.2}\text{Er}_{0.2}\text{Tm}_{0.2})_2(\text{WO}_4)_3$ high-entropy ceramic powder

La_2O_3 , CeO_2 , Gd_2O_3 , Er_2O_3 , Tm_2O_3 and WO_3 were weighed in stoichiometric amounts and placed in a zirconia jar for ball milling with ethanol and zirconia balls as the milling and grinding medium. The mass ratio of ball: powder was 5: 1. After milling at 400 rpm for 24 h, the mixture was fully dried at 80 °C. Then, the mixed powders were uniaxially pressed into cylindrical pellets, which were sintered at 900 °C for 12 h with a heating and cooling rate of 2 °C/min. Subsequently, the sintered product was crushed and subjected to the same high-energy ball milling procedure again. The final dried product was the required $(\text{La}_{0.2}\text{Ce}_{0.2}\text{Gd}_{0.2}\text{Er}_{0.2}\text{Tm}_{0.2})_2(\text{WO}_4)_3$ HEC powder.

2.3. Preparation of $(\text{La}_{0.2}\text{Ce}_{0.2}\text{Gd}_{0.2}\text{Er}_{0.2}\text{Tm}_{0.2})_2(\text{WO}_4)_3$ high-entropy ceramic powder/epoxy composite materials

First, 5 mL of n-butanol was added dropwise to 40 g of epoxy resin to reduce the viscosity of the epoxy resin so that the powder could be better dispersed. After continuous stirring, when the epoxy resin became transparent and flowed easily, 0 g, 8 g, 16 g and 32 g of high-entropy ceramic powder were slowly added. In this process, continuous stirring was required to reduce agglomeration. After stirring for approximately 0.5 h, 14.29 g of polyamide curing agent was added, and stirring was continued for approximately 0.5 h. Subsequently, the mixture was evenly poured into a polytetrafluoroethylene mold and placed in a vacuum drying oven for debubbling. After the bubbles were largely removed, the samples were placed at room temperature for curing for approximately 24 h. Here, for a simpler description, the materials with 0 g, 8 g, 16 g and 32 g of HEC powder were named EP, EP/W1, EP/W2 and EP/W3, whose corresponding powder mass fractions were 0%, 10.45%, 18.92% and 31.82%, respectively.

2.4. Characterization

The crystal structure and phase composition of the sample were identified by X-ray diffraction (XRD) using a Rigaku Miniflex 600 with Cu K α radiation at a scanning speed of 10°/min. The powder morphology was investigated by employing field emission scanning electron microscopy (SEM, Apreo S). The surface morphology of the sample was photographed by atomic force microscopy (AFM, NT-MDT). The particle size distribution curve of the $(\text{La}_{0.2}\text{Ce}_{0.2}\text{Gd}_{0.2}\text{Er}_{0.2}\text{Tm}_{0.2})_2(\text{WO}_4)_3$ HEC powder was examined using a multi-angle granularity high-sensitivity zeta potential analyzer (Brookhaven Omni); for this process, the powder was distributed in ultrapure water, and the testing temperature was 25 °C. The element distribution of the powder was determined by field emission transmission electron microscopy (TEM, FEI/Talos F200X G2) coupled with energy-dispersive spectroscopy (EDS). The mechanical properties of the $(\text{La}_{0.2}\text{Ce}_{0.2}\text{Gd}_{0.2}\text{Er}_{0.2}\text{Tm}_{0.2})_2(\text{WO}_4)_3$ /epoxy composite materials were studied using a universal testing machine (Instron 2365). The thermal conductivity of the samples was determined with a thermal constant analyzer (Hot Disk TPS 2200).

In this work, neutron radiography was used to detect the neutron shielding performance of the samples, and the thermal neutron absorption capacity of the samples was analyzed according to the change in the gray value around the image of the samples. During the experiment, a cadmium sheet with a thickness of 0.2 cm was used for comparison. The ambient humidity was 59%, and the temperature was 26 °C. The test results were provided by the Institute of Nuclear Energy Safety Technology, Hefei Institute of Material Science, Chinese Academy of Sciences.

The main detection equipment for γ -ray shielding was a dosimeter, and the detection radiation source included broad-spectrum filtered X-rays. The test environment temperature was 19.8 °C, the relative humidity was 68.6%, and the air pressure was 96.3 kPa. The test results were provided by the Testing and Calibration Laboratory of the Nuclear Powder Institute of China (NPIC).

3. Results and discussion

3.1. Phase composition and structural analysis of $(\text{La}_{0.2}\text{Ce}_{0.2}\text{Gd}_{0.2}\text{Er}_{0.2}\text{Tm}_{0.2})_2(\text{WO}_4)_3$

The phase composition and crystal structure of the $(\text{La}_{0.2}\text{Ce}_{0.2}\text{Gd}_{0.2}\text{Er}_{0.2}\text{Tm}_{0.2})_2(\text{WO}_4)_3$ powder calcined at 900 °C were deter-

mined through an analysis of the results shown in Fig. 1 (a), in which the XRD pattern of the $(\text{La}_{0.2}\text{Ce}_{0.2}\text{Gd}_{0.2}\text{Er}_{0.2}\text{Tm}_{0.2})_2(\text{WO}_4)_3$ powder was compared with those of $\text{La}_2(\text{WO}_4)_3$, $\text{Ce}_2(\text{WO}_4)_3$ and $\text{Gd}_2(\text{WO}_4)_3$ obtained from powder diffraction file (PDF) cards. In Fig. 1 (a), it can be clearly observed that the obtained powder matches the PDF card of $\text{Eu}_2(\text{WO}_4)_3$, which also shows that the as-synthesized single-phase tungstate has a monoclinic structure. Furthermore, because the average ion radius of these five rare earth ions is close to that of Eu(III), the structure of the $(\text{La}_{0.2}\text{Ce}_{0.2}\text{Gd}_{0.2}\text{Er}_{0.2}\text{Tm}_{0.2})_2(\text{WO}_4)_3$ powder obtained is close to that of $\text{Eu}_2(\text{WO}_4)_3$ [56,57], which coincides with the matching results from Jade software. After Rietveld refinement (Fullprof software [58–60], Fig. S1), the following unit cell data were determined. Fig. 1 (b) and Fig. S2 shows that the crystal structure of $(\text{La}_{0.2}\text{Ce}_{0.2}\text{Gd}_{0.2}\text{Er}_{0.2}\text{Tm}_{0.2})_2(\text{WO}_4)_3$ was monoclinic (C2/c), the lattice parameters were $(a, b, c) = (7.68004, 11.47247, 11.40990)$ and $(\alpha, \beta, \gamma) = (90.0, 109.73, 90.0)$, and the theoretical density = $7.356 \text{ g}\cdot\text{cm}^{-3}$. In addition, experiments have verified that the ratios of $\text{Er}_2(\text{WO}_4)_3$ and $\text{Tm}_2(\text{WO}_4)_3$ cannot be successfully synthesized, and there are no PDF cards of these two substances (Fig. S3). However, due to the greater lattice distortion effect and higher configuration entropy of HECs [31], these rare earth elements and tungsten together form a single phase and a material structure that may not otherwise exist.

3.2. Microstructure and element dispersion of samples

Fig. 2 (a) is an SEM image of the powder after ball milling. In combination with the particle size analysis (Fig. 2 (b)), it can be observed that $D_{50} = 1034.58 \text{ nm}$, and the particle size is relatively uniform. The powder in this case is beneficial to its dispersion in the epoxy resin matrix. Fig. 2 (c) is a representative TEM image of the synthesized HEC powder. At the lower end of the particle, an ordered lattice orientation can be seen, and the enlarged image (Fig. 2 (e)) shows multiple orientation lattices. The polycrystallinity of the particles is also verified by selected area electron diffraction (SAED), which shows spotty ring patterns, and there are no spots or rings in the second phase, which is consistent with the XRD data. Furthermore, in Fig. 2 (d), two positions were selected to calculate the lattice fringes. These two positions were verified to be the (113) and (040) crystal planes, for which the crystal plane spacings are 0.2790 nm and 0.2861 nm, respectively; the XRD calculation results of 0.2792 nm and 0.2870 nm are consistent with these values. The d-spacing and the corresponding planes identified from the diffraction rings are 0.3938 nm (022),

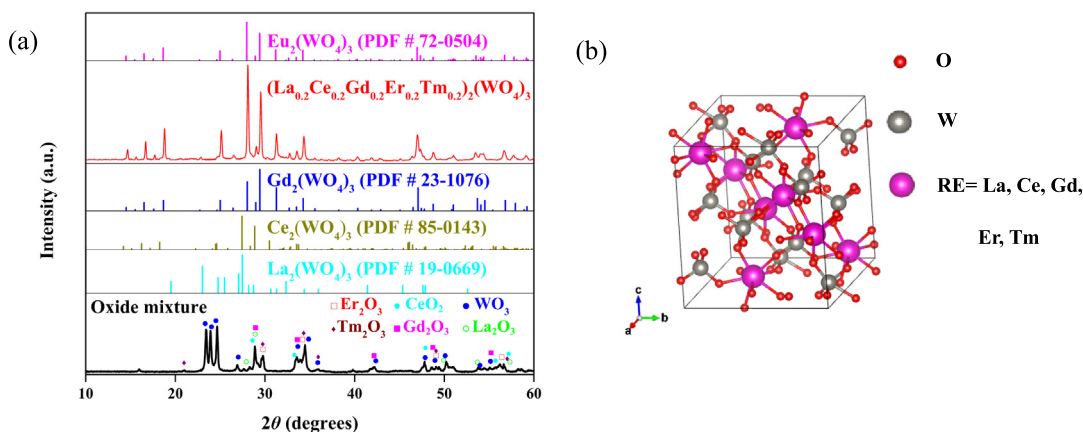


Fig. 1. (a) XRD patterns of the as-synthesized $(\text{La}_{0.2}\text{Ce}_{0.2}\text{Gd}_{0.2}\text{Er}_{0.2}\text{Tm}_{0.2})_2(\text{WO}_4)_3$ and those obtained from powder diffraction file (PDF) cards of $\text{La}_2(\text{WO}_4)_3$, $\text{Ce}_2(\text{WO}_4)_3$, $\text{Gd}_2(\text{WO}_4)_3$, $\text{Eu}_2(\text{WO}_4)_3$ and the oxide mixture (La_2O_3 , CeO_2 , Gd_2O_3 , Er_2O_3 , Tm_2O_3 , WO_3). (b) Crystal structure of $(\text{La}_{0.2}\text{Ce}_{0.2}\text{Gd}_{0.2}\text{Er}_{0.2}\text{Tm}_{0.2})_2(\text{WO}_4)_3$.

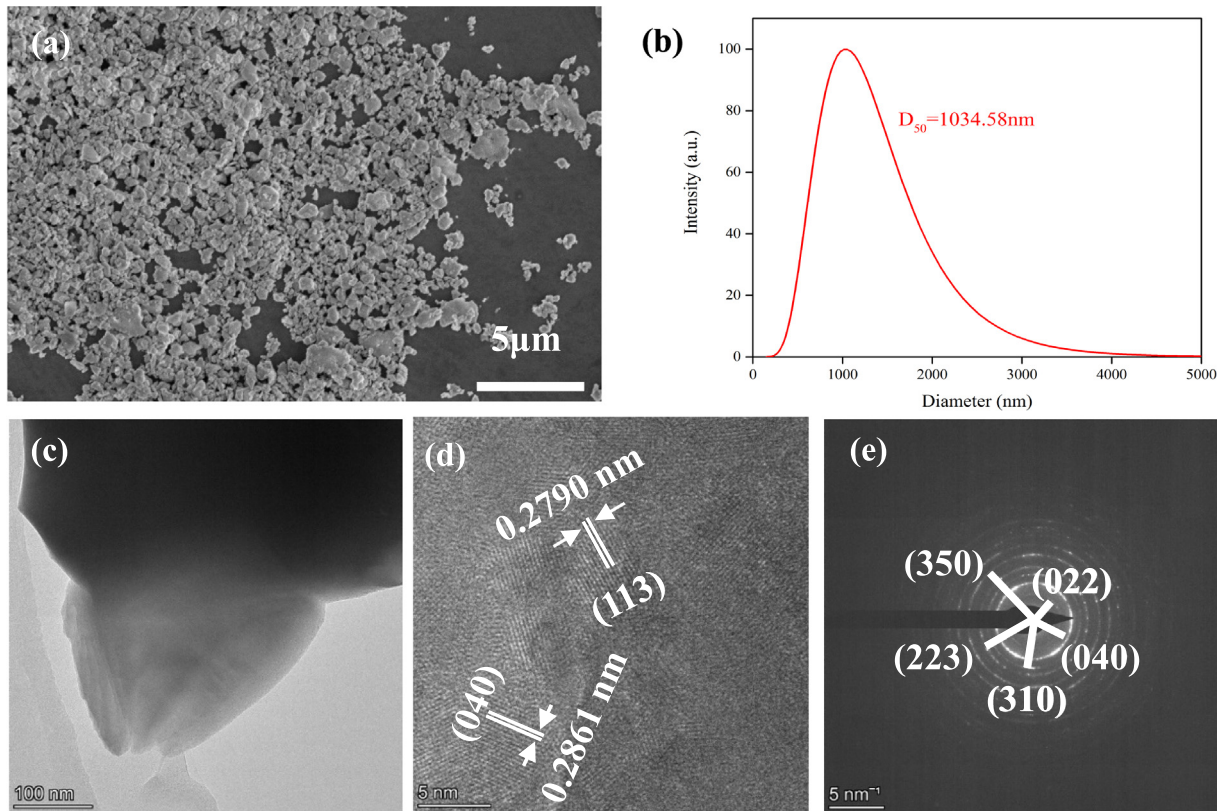


Fig. 2. (a) SEM image of the powder after high-energy ball milling, (b) particle size analysis curve, (c) TEM image, (d) high-resolution TEM image and (e) corresponding SAED pattern of the powder.

0.2866 nm (040), 0.2357 nm (310), 0.2060 nm (223) and 0.1667 nm (350). The diffraction angles of the remaining diffraction rings all exceed 60°, so they are not marked.

Fig. 3 and Fig. S4 show the surface morphology characterization of samples. Comparing Fig. 3 (a) and (d), clearly shows that a large amount of powder is uniformly distributed in EP/W3. Because the material itself is not conductive, the SEM imaging effect was limited. Therefore, to more clearly characterize the surface morphology, AFM was used [61–63]. Comparing Fig. 3 (b, c) and (e, f), the EP surface has more mountain-like protrusions, but the surfaces in EP/W3 are relatively short and more like hills. Fig. 3 (g) verified this phenomenon. The statistical calculation results show that the roughness of EP is 4.3335 nm and that of EP/W3 is 1.3723 nm. Interestingly, most of the pores in EP are small, but the pores in EP/W3 are very large. The reason is that because of the higher viscosity of EP/W3, the imprints left by the debubbling process are difficult to heal in a short time, which leads to the existence of large pores.

Fig. 4 presents a high-resolution TEM high-angle annular dark field (HAADF) image and corresponding selected compositional maps from EDS of the HEC powder to verify the uniformity of the elements in the powder. It can be clearly observed that all elements are uniformly dispersed without any segregation. The XRD analysis and SAED pattern results confirmed the formation of a single-phase solid solution. Combined with the above characteristics, HEC can be considered to have been formed.

3.3. Analysis of sample thermal neutron shielding data

The difference in grayscale in the neutron radiography image reflects the difference in the transmittance of thermal neutrons. For the image in Fig. 5, by selecting the center area (no smaller

than 50 × 50 pixels) of different samples, the average value of pixel gray was calculated to obtain the neutron imaging gray measurement value of different samples. In Fig. 5, the thermal neutron transmittance of the sample-free area is 1, which means total transmission. In contrast, cadmium has extremely high thermal neutron absorption capacity, so its thermal neutron transmittance (below the cadmium threshold) can be regarded as total absorption, with a value of 0. The neutron transmittance of other samples is between 0 and 1. The specific formula for calculating the thermal neutron transmittance of different samples in this work is Eq. (1).

$$\eta = \frac{GS_s - GS_C}{GS_B - GS_C} \quad (1)$$

where η is the thermal neutron transmittance, GS_s is the average gray value of the sample, GS_C is the average gray value of the 0.2 cm cadmium sheet, and GS_B is the average gray value of the film. Based on the above analysis and Eq. (1), the gray values of various materials and the calculation results of thermal neutron transmittance are listed in the 3rd and 4th columns of Table 1, respectively.

To eliminate the influence of sample thickness on the experimental data, the thermal neutron shielding data were calculated with an equivalent thickness of 2 cm. Eq. (2) is the formula for calculating the thermal neutron transmittance based on the macroscopic neutron capture cross section.

$$\eta = \frac{I}{I_0} = e^{-\Sigma d} \quad (2)$$

where η is the transmittance, I is the intensity of neutrons passing through the sample, I_0 is the intensity of incident neutrons, Σ (cm⁻¹) is the macroscopic neutron capture cross section, and d (cm) is the thickness of the sample.

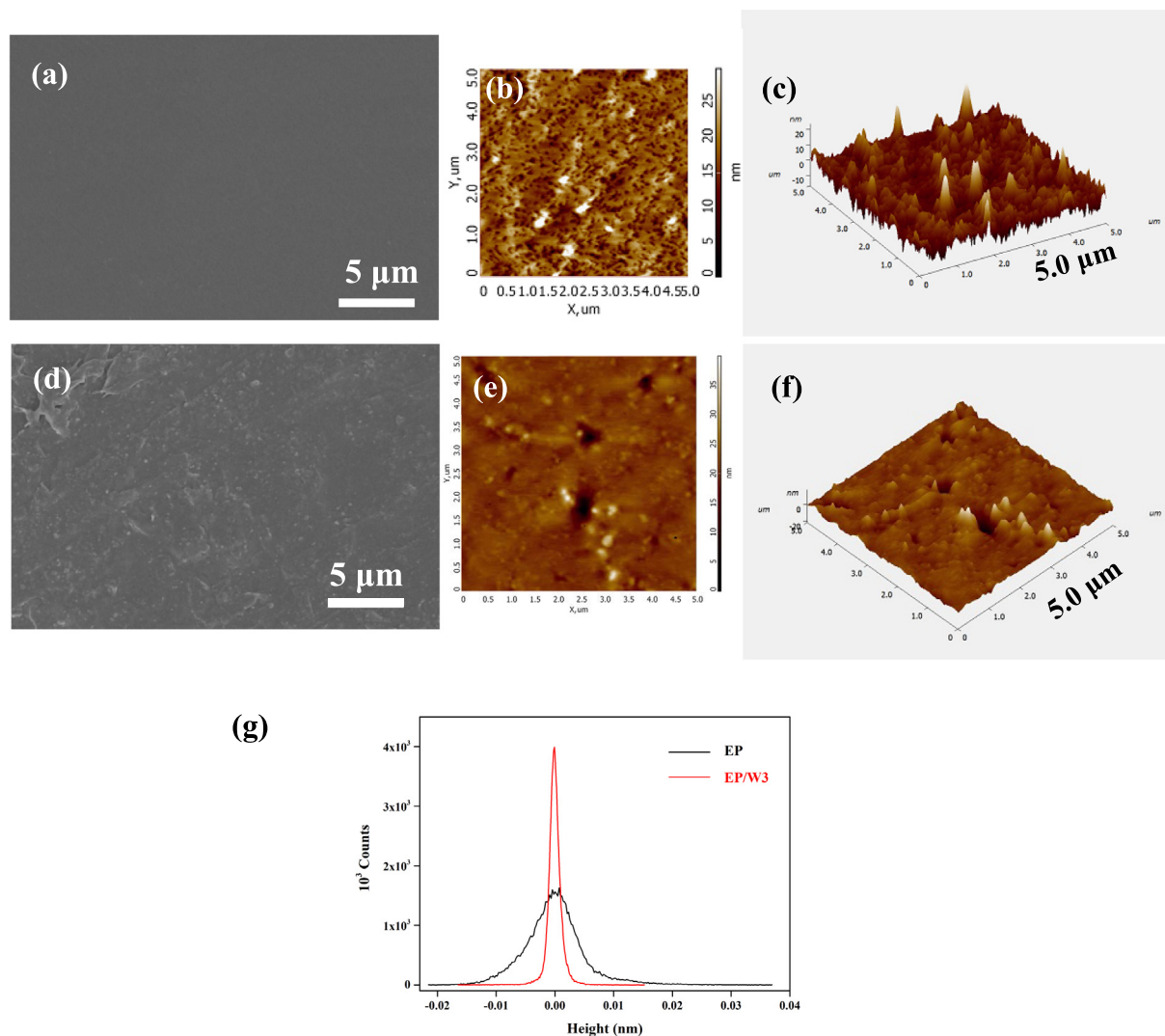


Fig. 3. (a–c) SEM, AFM-2D and AFM-3D images of the surface of EP; (d–f) SEM, AFM-2D and AFM-3D images of the surface of EP/W3; (g) height data curves of EP and EP/W3.

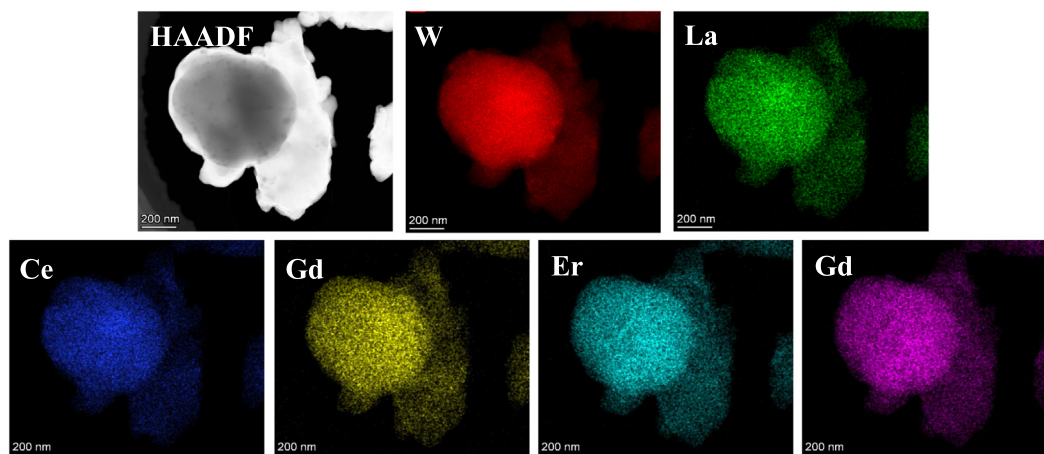


Fig. 4. High-resolution TEM high-angle annular dark field (HAADF) image of the powder and corresponding selected compositional maps from EDS.

For a specific sample material, the macroscopic capture cross section of thermal neutrons is constant. Therefore, according to Eq. (2), the neutron capture cross section of a material can be cal-

culated from the experimental value of the neutron transmittance of a sample with a certain thickness.

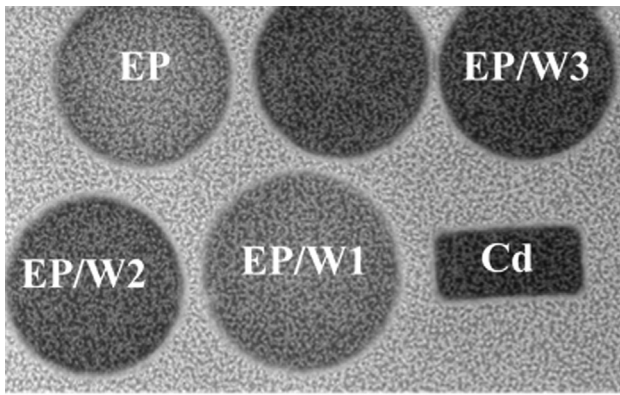


Fig. 5. Thermal neutron radiography images (the samples involved in this work have been marked).

Table 1

Data processing and analysis of the neutron radiography experiments.

Samples	Thickness (cm)	Average gray value	Experimental value of transmittance
Bottom plate	–	176.1	1
Cd	0.2	62.6	0
EP	0.739	150	0.770
EP/W1	0.562	137.7	0.662
EP/W2	0.780	111.2	0.428
EP/W3	0.784	77.5	0.131

$$\sum = -\frac{\ln(\eta)}{d} \quad (3)$$

Furthermore, **Eq. (4)** is the formula for calculating the thermal neutron transmittance for an equivalent thickness of 2 cm.

$$\eta_2 = \frac{I}{I_0} = e^{-\sum d} = e^{\frac{\ln(\eta)}{d} \times 2} \quad (4)$$

where η_2 is the transmittance of the 2-cm-thick sample, η is the experimental value of the transmittance, and d (cm) is the thickness of the sample. Based on **Eq. (4)**, the calculation results of the transmittance of the 2-cm-thick sample can be obtained, and the thermal neutron blocking efficiency of the 2-cm-thick sample can be further calculated. The specific material transmittance calculation results are shown in **Table 2**.

Through analysis of the data in **Table 2** and **Fig. 6**, it can be clearly seen that adding HEC powder significantly increases the thermal neutron blocking efficiency of the epoxy resin composite material from approximately 50% to nearly 100%. Compared with high-energy neutrons, moderated thermal neutrons are usually more easily absorbed by the material. Hydrogen is an effective element to slow neutrons. Therefore, the epoxy resin matrix containing a large amount of hydrogen has a certain thermal neutron absorption performance. The HEC powder mass in the EP/W3 sample with a 5-cm diameter and 2-cm thickness was calculated to be approximately 17.9822 g. This powder blocked approximately 50%

Table 2

Material transmittance calculation results.

Samples	Thickness (cm)	Mass fraction (%)	Experimental value of transmittance	Transmittance of 2-cm-thick samples	Barrier efficiency of 2-cm-thick samples (%)
EP	0.739	0	0.770	0.493	50.70
EP/W1	0.562	10.45	0.662	0.230	77.00
EP/W2	0.780	18.92	0.428	0.114	88.64
EP/W3	0.784	31.82	0.131	0.006	99.44

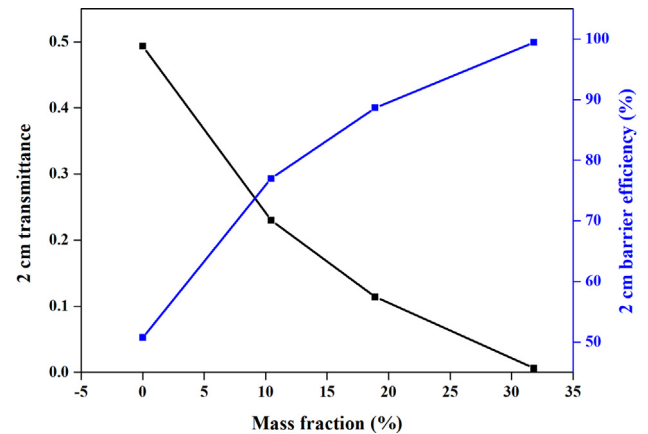


Fig. 6. Dotted-line graph of transmittance and blocking efficiency of different 2-cm-thick samples.

of thermal neutrons, which is equivalent to the blocking efficiency of over 40 g of EP.

The explanation for this phenomenon is as follows: First, rare earth elements have a large neutron capture cross section. In particular, Gd (35000 barns) has a larger neutron capture cross section than boron (730 barns), which is commonly used to absorb neutrons [64]. Second, rare earth elements have a unique atomic structure ordering, rich energy level transitions, relatively large atomic magnetic moments and strong spin-orbit coupling characteristics. Finally, as a potential substitute for lead, tungsten has positive application prospects in radiation protection materials. In the future, this experimental result can provide new ideas for reducing the weight requirements of radiation shielding materials.

In general, through doping HEC powder with a lower mass fraction, the shielding effect of the composite material is greatly improved, indicating that $(La_{0.2}Ce_{0.2}Gd_{0.2}Er_{0.2}Tm_{0.2})_2(WO_4)_3$ has favorable thermal neutron shielding performance.

3.4. Analysis of sample γ -ray shielding data

Table 3 shows the measured values of the γ -ray test. Based on the linear attenuation coefficient of γ -rays in the substance, the formula for calculating the attenuation ratio of the material to γ -rays is as follows:

$$\eta' = \frac{I_0'}{I} = e^{\mu' d'} \quad (5)$$

where η' is the attenuation ratio, I_0' is the incident γ -ray intensity, I is the γ -ray intensity passing through the sample, μ' (cm^{-1}) is the linear attenuation coefficient of the γ -ray in the material, and d' (cm) is the thickness of the sample.

For a specific sample material, the linear attenuation coefficient of γ -rays in the material is constant. Therefore, according to **Eq. (5)**, from the experimental value of the γ -ray attenuation ratio of the material with a specific thickness, the linear attenuation coefficient of γ -rays in the material can be calculated as follows:

Table 3
Sample data from the γ -ray shielding experiments.

Sample	EP	EP/W1	EP/W2	EP/W3
The average thickness (mm)	4.01	4.29	1.81	2.50
Energy (keV)	Attenuation ratio	Attenuation ratio	Attenuation ratio	Attenuation ratio
33	1.134	2.005	2.033	3.442
65	1.087	1.365	1.349	1.712
100	1.079	1.228	1.205	1.392
118	1.075	1.176	1.150	1.267
164	1.067	1.118	1.074	1.149
208	1.059	1.081	1.058	1.083
250	1.048	1.061	1.044	1.058

Table 4
Linear attenuation coefficient of different samples under different energy levels.

Linear attenuation coefficient μ' (cm^{-1})		Samples			
		EP	EP/W1	EP/W2	EP/W3
Energy (keV)	33	0.3136	1.6215	3.9200	4.9442
	65	0.2080	0.7253	1.6539	2.1506
	100	0.1896	0.4788	1.0303	1.3230
	118	0.1804	0.3780	0.7722	0.9466
	164	0.1617	0.2600	0.3944	0.5556
	208	0.1430	0.1816	0.3115	0.3189
	250	0.1169	0.1380	0.2379	0.2255

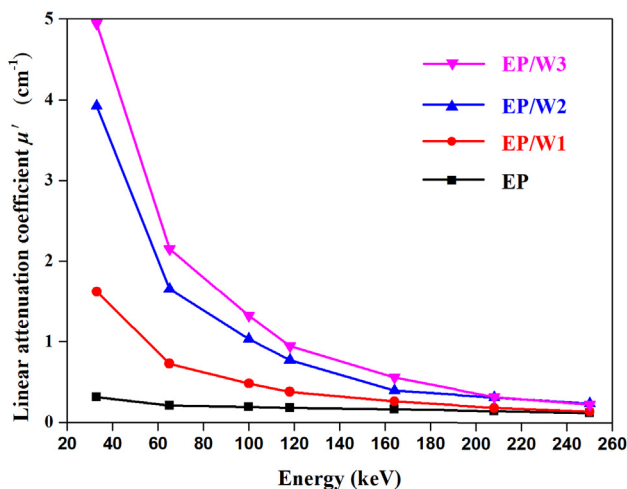


Fig. 7. Variation in the linear attenuation coefficient of different samples with increasing γ -ray energy.

$$\mu' = \frac{\ln(\eta')}{d} \quad (6)$$

From Eq. (6), the linear attenuation coefficients of different samples are calculated, and the results are shown in Table 4 and Fig. 7.

Table 4 and Fig. 7 show that as the powder doping increased, the linear attenuation coefficients in the low-energy and medium-energy regions increased significantly, whereas there was a relatively small change at 250 keV, mainly because the energy of γ -rays is too high for materials to shield them effectively. Nevertheless, although the linear attenuation coefficient was reduced, the lead equivalent value exhibited an increasing trend, which will be discussed subsequently. This phenomenon indicates that increasing the amount of HEC powder added can improve the degree of protection against γ -rays. In the material preparation, the amount of powder in EP cannot be increased indefinitely. In this case, appropriately increasing the material thickness is more

conductive to the shielding effect. However, at 208 and 250 keV, the linear attenuation coefficient does not change significantly. This phenomenon may be caused by the increase in the amount of powder doping, which increases the oxygen vacancies in the material, thereby weakening the shielding performance of the material against γ -rays.

The linear attenuation coefficient of EP/W3 is more than ten times greater than that of EP at 33 keV and 65 keV. Although the ratio decreases as the γ -ray energy becomes larger, it is always greater than two. This performance difference indicates that the doped HEC powder plays a more important role in shielding γ -rays than the epoxy resin used as the matrix for testing the sample performance.

Table 5 shows the linear attenuation coefficients of some materials reported in recent papers. By comparison with the data in this work, it can be observed that $(\text{La}_{0.2}\text{Ce}_{0.2}\text{Gd}_{0.2}\text{Er}_{0.2}\text{Tm}_{0.2})_2(\text{WO}_4)_3$ has a higher linear attenuation coefficient than these commonly used materials. It is positively proven that the materials designed in this work have advantages.

Subsequently, to highlight the advantage of $(\text{La}_{0.2}\text{Ce}_{0.2}\text{Gd}_{0.2}\text{Er}_{0.2}\text{Tm}_{0.2})_2(\text{WO}_4)_3$ in the lead feeble absorbing area, the lead equivalent was calculated. It can be observed from Table 6 and Fig. 8 that when the γ -ray energy is 65 keV, the lead equivalent value increases significantly, indicating that the doped rare earth HEC powder has an outstanding shielding effect against γ -rays near this energy level. This is because the k-edge of rare earth elements (listed in Table 7) increases with increasing atomic number, which basically covers the lead feeble absorbing area [49,51]. Furthermore, when rare earth elements form compounds, 4f, 5d, 6s, and 6p can all be used as valence orbitals, and the valence electrons of rare earth elements have the advantage of covering a large space, which can shield γ -rays by enhancing the Compton effect. However, with increasing γ -ray energy, the shielding performance of the material drops, which is similar to the trend in the shielding effect of lead-based materials in the middle- and low-energy regions. In addition, Table 8 lists the number of W atoms and rare earth atoms per unit volume and shows that as the number of doping increases, the tungsten and rare earth elements contained in the composite material also increase significantly, further confirm-

Table 5

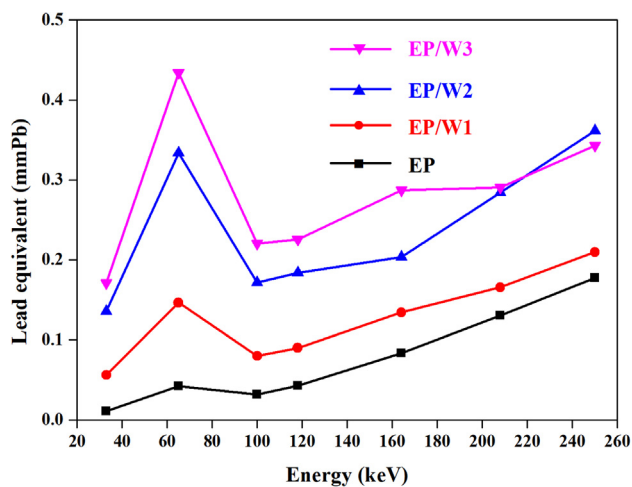
Reported linear attenuation coefficient of composites under different energy levels.

Sample	Filler (wt ₁ %–wt ₂ %)	Energy (keV)	Linear attenuation coefficient (cm ⁻¹)	References
EP/W1	10.45	65	0.7253	This work
EP/W2	18.92	65	1.6539	
EP/W3	31.82	65	2.1506	
Epoxy-Ta ₂ O ₅	10	59.65	0.6115	[20]
	20	59.65	0.9709	
	30	59.65	1.2915	
Epoxy-Ta ₂ O ₅ -Bi ₂ O ₃	5–5	59.65	0.7161	[20]
	5–30	59.65	1.9647	
	0–35	59.65	2.0716	
EP/W2	18.92	118	0.7722	This work
EP/W3	31.82	118	0.9466	
Epoxy-HfO ₂	30	122	0.8895	
Epoxy-WO ₃	30	122	0.8801	[1]
Polymer-W-B ₄ C	10–8	122	0.4300	
	18–12	122	0.7300	

Table 6

Lead equivalent values of 1-cm-thick samples at different energy levels.

Lead equivalent (mmPb)		1-cm-thick samples			
		EP	EP/W1	EP/W2	EP/W3
Energy (keV)	33	0.01083	0.05601	0.13540	0.17078
	65	0.04198	0.14638	0.33379	0.43404
	100	0.03160	0.07979	0.17171	0.22049
	118	0.04294	0.08998	0.18385	0.22538
	164	0.08353	0.13430	0.20373	0.28697
	208	0.13038	0.16558	0.28409	0.29088
	250	0.17768	0.20976	0.36155	0.34274

**Fig. 8.** Changes of the lead equivalent values of 1-cm-thick samples under different energy levels.**Table 7**

K-edge data of the elements used in this work.

Element	La	Ce	Gd	Er	Tm	W
K-edge (keV)	38.932	40.452	50.232	57.484	59.376	69.525

Table 8Number of tungsten atoms and rare earth atoms in 1 cm³ samples.

Sample	Density (g·cm ⁻³)	Mass fraction	1 cm ³ sample		
			The amount of substance of powder (mol)	The number of tungsten atoms	The number of rare earth atoms
EP/W1	1.2109	0.1045	1.20×10^4	2.1713×10^{20}	1.4475×10^{20}
EP/W2	1.2865	0.1862	2.28×10^4	4.1104×10^{20}	2.7403×10^{20}
EP/W3	1.4398	0.3182	4.35×10^4	7.8613×10^{20}	5.2409×10^{20}

Table 9

Thermal conductivity, density, and tensile strength of the samples.

Samples	Thermal conductivity (W·m ⁻¹ ·K ⁻¹)	Density (g·cm ⁻³)	Tensile strength (MPa)
EP	0.2335	1.0889	18.16
EP/W1	0.2301	1.2109	17.23
EP/W2	0.2577	1.2865	11.76
EP/W3	0.2956	1.4398	19.25

ing that the doping of HEC powder containing tungsten and rare earth elements is an important factor in improving the radiation protection performance of composite materials.

In summary, the (La_{0.2}Ce_{0.2}Gd_{0.2}Er_{0.2}Tm_{0.2})₂(WO₄)₃ material prepared in this work has promising γ -ray shielding performance. Furthermore, because rare earth elements can effectively protect against 40–88 keV γ -rays, combining the characteristics of the materials in this work with the advantages of lead-based materials to effectively protect against low- and medium-energy X-rays used

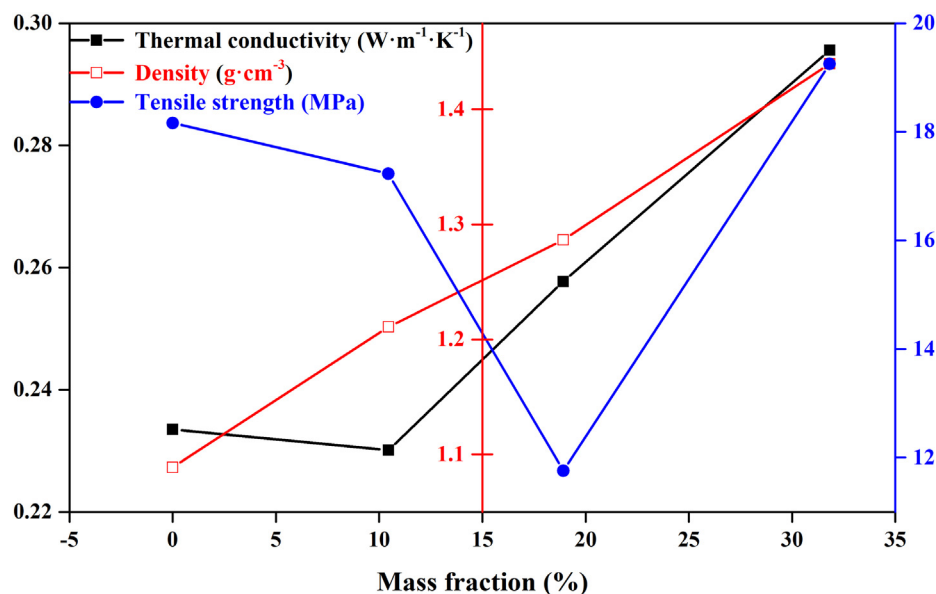


Fig. 9. Changes in thermal conductivity, density and tensile strength with increasing powder mass fraction.

in medical or industrial applications compensates for the feeble absorbing area of lead-based materials.

3.5. Thermal conductivity, density and tensile properties of the samples

The properties mentioned in Table 9 are all related to the amount of powder added to the epoxy. To observe the influence of the powder mass fraction on these physical properties more intuitively, a dotted-line graph was made, as shown in Fig. 9. In terms of thermal conductivity, the thermal conductivity of EP/W1 is slightly lower than that of epoxy. The reason is that the addition of powder increases the number of pores in the material, resulting in a slight decrease in thermal conductivity at room temperature. The thermal conductivity of EP/W1, EP/W2, and EP/W3 increases with increasing powder mass fraction because the thermal conductivity of the powder is significantly higher than that of epoxy. This same trend is found for the sample density because the density of the powder is higher than that of epoxy, so the sample density increases as the powder mass fraction increases.

The fourth column in Table 9 and Fig. 9 shows that the tensile strength first decreases and then increases with increasing powder mass fraction. This phenomenon occurs because the tensile strength is dominated by the epoxy when the powder mass fraction is low. Hence, when a small amount of powder is added, it disrupts the connections between the epoxy, leading to a decrease in tensile strength. However, when the powder mass fraction is high, the tensile strength is dominated by the powder, which is stronger than the epoxy. Thus, as the powder mass fraction subsequently increases, the tensile strength increases. In practical applications, the composite materials can be used as coating on the surface of the equipment, or processed into the required form according to the actual needs. Because composite materials are easy to process, the requirements for tensile properties are greatly reduced. In addition, the substrate used in this work has certain flame retardancy, which is very important for the safety of nuclear equipment. Of course, in future work, the mechanical properties of composite materials will be further optimized to adapt to more application environments [66,67].

4. Conclusion

In this work, a novel monoclinic-type high-entropy rare earth tungstate ceramic, $(\text{La}_{0.2}\text{Ce}_{0.2}\text{Gd}_{0.2}\text{Er}_{0.2}\text{Tm}_{0.2})_2(\text{WO}_4)_3$, was designed and synthesized by a high-temperature solid-phase method. The as-prepared powder had a polycrystalline orientation and uniform element dispersion, and the powder particles after ball milling were relatively uniform. The composite materials formed by dispersing different amounts of the powder in epoxy resin had acceptable tensile strength (>10 MPa), relatively low thermal conductivity (<0.3 W·m⁻¹·K⁻¹) and relatively low density (<1.5 g·cm⁻³). When doped with a powder mass fraction of approximately 32%, the thermal neutron absorption rate of EP approximately doubled, and nearly 100% of thermal neutrons could be shielded due to the high neutron capture cross section of rare earth elements. Moreover, the material had outstanding shielding properties in the whole range of low- and medium-energy γ -rays. When the energy was 65 keV, the lead equivalent value significantly increased, indicating that the material has typical shielding performance in the feeble absorbing area of lead-based and bismuth-based materials, showing the utility of the five rare earth elements selected in the experimental design. In addition, the high toxicity problem of lead-based materials can be easily solved, and the high configuration entropy can better stabilize the structure and reduce the negative effects of changes in the crystal form after radiation. Therefore, the $(\text{La}_{0.2}\text{Ce}_{0.2}\text{Gd}_{0.2}\text{Er}_{0.2}\text{Tm}_{0.2})_2(\text{WO}_4)_3$ material designed in this work solves some problems in the application of radiation protection materials and provides a candidate for shielding thermal neutrons and low- and medium-energy γ -rays.

Declaration of Competing Interest

The authors declare that they have no known competing financial interests or personal relationships that could have appeared to influence the work reported in this paper.

Acknowledgements

This work was supported financially by the "Transformational Technologies for Clean Energy and Demonstration", Strategic Prior-

ity Research Program of the Chinese Academy of Sciences, Grant No. XDA21000000.), the 2020 Opening Foundation of State Key Laboratory of Baiyunobo Rare Earth Resource Researches and Comprehensive Utilization (2020Z2117), the Science and Technology Projects of Xiamen (3502Z20193080), the National Key Research and Development Program of China (No. 2019YFC0605000) and the FJIRSM&IUE Joint Research Fund (No. RHZX-2018-001). In addition, we are grateful to the Institute of Nuclear Energy Safety Technology, Hefei Institute of Material Science, Chinese Academy of Sciences and the Science and Technology on Reactor System Design Technology Laboratory of NPIC for their support in analysis and testing.

Appendix A. Supplementary material

Supplementary data to this article can be found online at <https://doi.org/10.1016/j.matdes.2021.109722>.

References

- [1] M.C. Molina Higgins, N.A. Radcliffe, M. Toro-González, J.V. Rojas, Gamma ray attenuation of hafnium dioxide- and tungsten trioxide-epoxy resin composites, *J. Radioanal. Nucl. Chem.* 322 (2) (2019) 707–716.
- [2] M.R. Kacal, F. Akman, M.I. Sayyed, Investigation of radiation shielding properties for some ceramics, *Radiochim. Acta* 107 (2) (2019) 179–191.
- [3] A. Anshul, S.S. Amritphale, N. Chandra, N. Ramakrishnan, A. Shrivastava, U.S.P. Verma, Chemically formulated ceramic gamma ray irradiation shielding materials utilising red mud, *Adv. Appl. Ceram.* 108 (7) (2013) 429–437.
- [4] M. Erdem, O. Baykara, M. Doğru, F. Kuluöztürk, A novel shielding material prepared from solid waste containing lead for gamma ray, *Radiat. Phys. Chem.* 79 (9) (2010) 917–922.
- [5] D. Rezaei-Ochbelagh, S. Azimkhani, Investigation of gamma-ray shielding properties of concrete containing different percentages of lead, *Appl. Radiat. Isot.* 70 (10) (2012) 2282–2286.
- [6] E. Şakar, M. Büyükyıldız, B. Alım, B.C. Şakar, M. Kurudirek, Lead brass alloys for gamma-ray shielding applications, *Radiat. Phys. Chem.* 159 (2019) 64–69.
- [7] W. Huang, W. Yang, Q. Ma, J. Wu, J. Fan, K. Zhang, Preparation and characterization of γ -ray radiation shielding PbWO_4 /EPDM composite, *J. Radioanal. Nucl. Chem.* 309 (3) (2016) 1097–1103.
- [8] S.R. Manohara, S.M. Hanagodimath, L. Gerward, Photon interaction and energy absorption in glass: A transparent gamma ray shield, *J. Nucl. Mater.* 393 (3) (2009) 465–472.
- [9] I. Akkurt, H. Akyildirim, B. Mavi, S. Kilincarslan, C. Basyigit, Gamma-ray shielding properties of concrete including barite at different energies, *Prog. Nucl. Energy* 52 (7) (2010) 620–623.
- [10] B. Pomaro, F. Gramegna, R. Cherubini, V. De Nadal, V. Salomoni, F. Faleschini, Gamma-ray shielding properties of heavyweight concrete with Electric Arc Furnace slag as aggregate: An experimental and numerical study, *Constr. Build. Mater.* 200 (2019) 188–197.
- [11] E. Horszczaruk, P. Brzozowski, Investigation of gamma ray shielding efficiency and physicochemical performances of heavyweight concrete subjected to high temperature, *Constr. Build. Mater.* 195 (2019) 574–582.
- [12] Y.-C. Xu, C. Song, X.-Y. Ding, Y. Zhao, D.-G. Xu, Q.-P. Zhang, Y.-L. Zhou, Tailoring lattices of Bi_2WO_6 crystals via Ce doping to improve the shielding properties against low-energy gamma rays, *J. Phys. Chem. Solids* 127 (2019) 76–80.
- [13] M.V. Muthamma, S.G. Bubbly, S.B. Gudennavar, Attenuation properties of epoxy- Ta_2O_5 and epoxy- Ta_2O_5 - Bi_2O_3 composites at γ -ray energies 59.54 and 662 keV, *J. Appl. Polym. Sci.* (2020) 49366.
- [14] H. Alavian, A. Samie, H. Tavakoli-Anbaran, Experimental and Monte Carlo investigations of gamma ray transmission and buildup factors for inorganic nanoparticle/epoxy composites, *Radiat. Phys. Chem.* 174 (2020) 108960.
- [15] H. Zhang, R. Qi, M. Tong, Y. Su, M. Huang, In situ solvothermal synthesis and characterization of transparent epoxy/ TiO_2 nanocomposites, *J. Appl. Polym. Sci.* 125 (2) (2012) 1152–1160.
- [16] R. Adeli, S.P. Shirmardi, S.J. Ahmadi, Neutron irradiation tests on B_4C /epoxy composite for neutron shielding application and the parameters assay, *Radiat. Phys. Chem.* 127 (2016) 140–146.
- [17] L. Chang, Y. Zhang, Y. Liu, J. Fang, W. Luan, X. Yang, W. Zhang, Preparation and characterization of tungsten/epoxy composites for γ -rays radiation shielding, *Nucl. Instrum. Methods Phys. Res. Sect. B* 356–357 (2015) 88–93.
- [18] Z.M. Tsikriteas, G.C. Manika, A.C. Patsidis, G.C. Psarras, Probing the multifunctional behaviour of barium zirconate/barium titanate/epoxy resin hybrid nanodielectrics, *J. Therm. Anal. Calorim.* (2020).
- [19] M. Jamil, M.H. Hazlan, R.M. Ramli, N.Z. Noor Azman, Study of electrospun PVA-based concentrations nanofibre filled with Bi_2O_3 or WO_3 as potential x-ray shielding material, *Radiat. Phys. Chem.* 156 (2019) 272–282.
- [20] J.W. Shin, J.-W. Lee, S. Yu, B.K. Baek, J.P. Hong, Y. Seo, W.N. Kim, S.M. Hong, C.M. Koo, Polyethylene/boron-containing composites for radiation shielding, *Thermochim. Acta* 585 (2014) 5–9.
- [21] Y. Wu, J. Hu, C. Feng, G. Chen, J. Yang, Carborane-containing copolyester fibers with unique neutron shielding properties, *Mater. Des.* 172 (2019) 10772.
- [22] T. Hayashi, K. Tobita, Y. Nakamori, S. Orimo, Advanced neutron shielding material using zirconium borohydride and zirconium hydride, *J. Nucl. Mater.* 386–388 (2009) 119–121.
- [23] K.A. Dubey, C.V. Chaudhari, S.K. Suman, N. Raje, R.K. Mondal, V. Grover, S. Murali, Y.K. Bhardwaj, L. Varshney, Synthesis of flexible polymeric shielding materials for soft gamma rays: Physicochemical and attenuation characteristics of radiation crosslinked polydimethylsiloxane/ Bi_2O_3 composites, *Polym. Compos.* 37 (3) (2016) 756–762.
- [24] J. Kaewkhao, A. Pokaipisit, P. Limsuwan, Study on borate glass system containing with Bi_2O_3 and BaO for gamma-rays shielding materials: Comparison with PbO , *J. Nucl. Mater.* 399 (1) (2010) 38–40.
- [25] R. Li, Y. Gu, Y. Wang, Z. Yang, M. Li, Z. Zhang, Effect of particle size on gamma radiation shielding property of gadolinium oxide dispersed epoxy resin matrix composite, *Mater. Res. Express* 4 (3) (2017) 035035.
- [26] A.T. Anishur Rahman, K. Vasilev, P. Majewski, Ultra small Gd_2O_3 nanoparticles: Absorption and emission properties, *J. Colloid Interface Sci.* 354 (2) (2011) 592–596.
- [27] P.K. Kulriya, T. Yao, S.M. Scott, S. Nanda, J. Lian, Influence of grain growth on the structural properties of the nanocrystalline $\text{Gd}_2\text{Ti}_2\text{O}_7$, *J. Nucl. Mater.* 487 (2017) 373–379.
- [28] R.Z. Zhang, M.J. Reece, Review of high entropy ceramics: design, synthesis, structure and properties, *J. Mater. Chem. A* 7 (39) (2019) 22148–22162.
- [29] M. Zhang, X. Xu, Y. Yue, M. Palma, M.J. Reece, H. Yan, Multi elements substituted Aurivillius phase relaxor ferroelectrics using high entropy design concept, *Mater. Des.* 200 (2021) 109447.
- [30] S.H. Albedwawi, A. Aljaberi, G.N. Haidemenopoulos, K. Polychronopoulou, High entropy oxides-exploring a paradigm of promising catalysts: a review, *Mater. Des.* 202 (2021) 109534.
- [31] C.M. Rost, E. Sachet, T. Borman, A. Moballegh, E.C. Dickey, D. Hou, J.L. Jones, S. Curtarolo, J.P. Maria, Entropy-stabilized oxides, *Nat. Commun.* 6 (2015) 8485.
- [32] R. Djenadic, A. Sarkar, O. Clemens, C. Loho, M. Botros, V.S.K. Chakravadhanula, C. Kübel, S.S. Bhattacharya, A.S. Gandhi, H. Hahn, Multicomponent equiatomic rare earth oxides, *Mater. Res. Lett.* 5 (2) (2016) 102–109.
- [33] J. Gild, M. Samiee, J.L. Braun, T. Harrington, H. Vega, P.E. Hopkins, K. Vecchio, J. Luo, High-entropy fluorite oxides, *J. Eur. Ceram. Soc.* 38 (10) (2018) 3578–3584.
- [34] L. Spiridigliizzi, C. Ferone, R. Cioffi, G. Dell'Agli, A simple and effective predictor to design novel fluorite-structure high entropy oxides (HEOs), *Acta Mater.* 202 (2021) 181–189.
- [35] S. Jiang, T. Hu, J. Gild, N. Zhou, J. Nie, M. Qin, T. Harrington, K. Vecchio, J. Luo, A new class of high-entropy perovskite oxides, *Scr. Mater.* 142 (2018) 116–120.
- [36] X. Zhang, L. Xue, F. Yang, Z. Shao, H. Zhang, Z. Zhao, K. Wang, $(\text{La}_{0.2}\text{Y}_{0.2}\text{Nd}_{0.2}\text{Gd}_{0.2}\text{Sr}_{0.2})\text{CrO}_3$: A novel conductive porous high-entropy ceramic synthesized by the sol-gel method, *J. Alloys Compd.* 863 (2021) 158763.
- [37] A. Sarkar, R. Djenadic, D. Wang, C. Hein, R. Kautenburger, O. Clemens, H. Hahn, Rare earth and transition metal based entropy stabilised perovskite type oxides, *J. Eur. Ceram. Soc.* 38 (5) (2018) 2318–2327.
- [38] J. Dąbrowa, M. Stygar, A. Mikula, A. Knapik, K. Mroczka, W. Tejchman, M. Danielewski, M. Martin, Synthesis and microstructure of the (Co, Cr, Fe, Mn, Ni) $_{304}$ high entropy oxide characterized by spinel structure, *Mater. Lett.* 216 (2018) 32–36.
- [39] Z. Zhao, H. Chen, H. Xiang, F.-Z. Dai, X. Wang, W. Xu, K. Sun, Z. Peng, Y. Zhou, $(\text{Y}_{0.25}\text{Yb}_{0.25}\text{Er}_{0.25}\text{Lu}_{0.25})_2(\text{Zr}_{0.5}\text{Hf}_{0.5})_2\text{O}_7$: A defective fluorite structured high entropy ceramic with low thermal conductivity and close thermal expansion coefficient to Al_2O_3 , *J. Mater. Sci. Technol.* 39 (2020) 167–172.
- [40] Z. Zhao, H. Xiang, F.-Z. Dai, Z. Peng, Y. Zhou, $(\text{La}_{0.2}\text{Ce}_{0.2}\text{Nd}_{0.2}\text{Sm}_{0.2}\text{Eu}_{0.2})_2\text{Zr}_2\text{O}_7$: A novel high-entropy ceramic with low thermal conductivity and sluggish grain growth rate, *J. Mater. Sci. Technol.* 35 (11) (2019) 2647–2651.
- [41] H. Chen, H. Xiang, F.-Z. Dai, J. Liu, Y. Zhou, Porous high entropy $(\text{Zr}_{0.2}\text{Hf}_{0.2}\text{Ti}_{0.2}\text{Nb}_{0.2}\text{Ta}_{0.2})\text{B}_2$: A novel strategy towards making ultrahigh temperature ceramics thermal insulating, *J. Mater. Sci. Technol.* 35 (10) (2019) 2404–2408.
- [42] H. Chen, Z. Zhao, H. Xiang, F.-Z. Dai, J. Zhang, S. Wang, J. Liu, Y. Zhou, Effect of reaction routes on the porosity and permeability of porous high entropy $(\text{Y}_{0.2}\text{Yb}_{0.2}\text{Sm}_{0.2}\text{Nd}_{0.2}\text{Eu}_{0.2})\text{B}_6$ for transpiration cooling, *J. Mater. Sci. Technol.* 38 (2020) 80–85.
- [43] J. Gild, Y. Zhang, T. Harrington, S. Jiang, T. Hu, M.C. Quinn, W.M. Mellor, N. Zhou, K. Vecchio, J. Luo, High-entropy metal diborides: a new class of high-entropy materials and a new type of ultrahigh temperature ceramics, *Sci. Rep.* 6 (2016) 37946.
- [44] D.G. Sangiovanni, F. Tasnádi, T. Harrington, M. Odén, K.S. Vecchio, I.A. Abrikosov, Temperature-dependent elastic properties of binary and multicomponent high-entropy refractory carbides, *Mater. Des.* 204 (2021) 109634.
- [45] B. Du, H. Liu, Y. Chu, Fabrication and characterization of polymer-derived high-entropy carbide ceramic powders, *J. Am. Ceram. Soc.* 103 (8) (2020) 4063–4068.
- [46] T.J. Harrington, J. Gild, P. Sarker, C. Toher, C.M. Rost, O.F. Dippo, C. McElfresh, K. Kauffmann, E. Marin, L. Borowski, P.E. Hopkins, J. Luo, S. Curtarolo, D.W. Brenner, K.S. Vecchio, Phase stability and mechanical properties of novel high entropy transition metal carbides, *Acta Mater.* 166 (2019) 271–280.
- [47] T. Jin, X. Sang, R.R. Unocic, R.T. Kinch, X. Liu, J. Hu, H. Liu, S. Dai, Mechanochemical-assisted synthesis of high-entropy metal nitride via a soft urea strategy, *Adv. Mater.* 30 (23) (2018) 1707512.

- [48] Y. Qin, J.C. Wang, J.X. Liu, X.F. Wei, F. Li, G.J. Zhang, C. Jing, J. Zhao, H. Wu, High-entropy silicide ceramics developed from (TiZrNbMoW)Si₂ formulation doped with aluminum, *J. Eur. Ceram. Soc.* 40 (8) (2020) 2752–2759.
- [49] F. Wang, X. Yan, T. Wang, Y. Wu, L. Shao, M. Nastasi, Y. Lu, B. Cui, Irradiation damage in (Zr_{0.25}Ta_{0.25}Nb_{0.25}Ti_{0.25})C high-entropy carbide ceramics, *Acta Mater.* 195 (2020) 739–749.
- [50] M.A. Marzouk, H.A. ElBatal, A.M. Abdelghany, Gamma irradiation effect on structural and spectral properties of CeO₂, Nd₂O₃, Gd₂O₃ or Dy₂O₃-doped strontium borate glass, *Silicon* 10 (1) (2017) 29–37.
- [51] P. Kaur, D. Singh, T. Singh, Sm³⁺ and Gd³⁺ Co-doped lead phosphate glasses for γ -rays shielding and sensing, *J. Lumin.* 209 (2019) 74–88.
- [52] K.M. Mahmoud, Y.S. Rammah, Investigation of gamma-ray shielding capability of glasses doped with Y, Gd, Nd, Pr and Dy rare earth using MCNP-5 code, *Phys. B* 577 (2020) 411756.
- [53] D. Yilmaz, B. Aktaş, Ş. Yalçın, M. Albaşkara, Erbium oxide and cerium oxide-doped borosilicate glasses as radiation shielding material, *Radiat. Eff. Defects in Solids* 175 (5–6) (2019) 458–471.
- [54] E.A. Potanina, A.I. Orlova, D.A. Mikhailov, A.V. Nokhrin, V.N. Chuvil'deev, M.S. Boldin, N.V. Sakharov, E.A. Lantsev, M.G. Tokarev, A.A. Murashov, Spark plasma sintering of fine-grained SrWO₄ and NaNd(WO₄)₂ tungstates ceramics with the scheelite structure for nuclear waste immobilization, *J. Alloys Compd.* 774 (2019) 182–190.
- [55] R. Li, Y. Gu, Z. Yang, M. Li, Y. Hou, Z. Zhang, Gamma ray shielding property, shielding mechanism and predicting model of continuous basalt fiber reinforced polymer matrix composite containing functional filler, *Mater. Des.* 124 (2017) 121–130.
- [56] Y. Pu, Q. Zhang, R. Li, M. Chen, X. Du, S. Zhou, Dielectric properties and electrocaloric effect of high-entropy (Na_{0.2}Bi_{0.2}Ba_{0.2}Sr_{0.2}Ca_{0.2})TiO₃ ceramic, *Appl. Phys. Lett.* 115 (22) (2019) 223901.
- [57] D.H. Templeton, A. Zalkin, Crystal structure of europium tungstate, *Acta Cryst.* 16 (1963) 762–766.
- [58] K. Shan, F. Zhai, Z.Z. Yi, X.T. Yin, D. Dastan, F. Tajabadi, A. Jafari, S. Abbasi, Mixed conductivity and the conduction mechanism of the orthorhombic CaZrO₃ based materials, *Surf. Interfaces* 23 (2021) 100905.
- [59] K. Shan, Z.Z. Yi, X.T. Yin, L. Cui, D. Dastan, H. Garmestani, F.M. Alamgir, Diffusion kinetics mechanism of oxygen ion in dense diffusion barrier limiting current oxygen sensors, *J. Alloys Compd.* 855 (2021) 157465.
- [60] K. Shan, Z.Z. Yi, X.T. Yin, D. Dastan, S. Dadkhah, B.T. Coates, H. Garmestani, Mixed conductivities of A-site deficient Y, Cr-doubly doped SrTiO₃ as novel dense diffusion and temperature-independent limiting current oxygen sensors, *Adv. Powder Technol.* 31 (2020) 4657–4664.
- [61] Ş. Tâlu, S. Kulesza, M. Bramowicz, K. Stepień, D. Dastan, Analysis of the surface microtexture of sputtered indium tin oxide thin films, *Arch. Metall. Mater.* 66 (2) (2021) 443–450.
- [62] A. Jafari, K. Tahani, D. Dastan, S. Asgari, Z. Shi, X.T. Yin, W.D. Zhou, H. Garmestani, Ş. Tâlu, Ion implantation of copper oxide thin films; statistical and experimental results, *Surf. Interfaces* 18 (2020) 100463.
- [63] R. Shakoury, A. Arman, Ş. Tâlu, D. Dastan, C. Luna, S. Rezaee, Stereometric analysis of TiO₂ thin films deposited by electron beam ion assisted, *Opt. Quantum Electron.* 52 (2020) 270.
- [64] H. Pomerance, Thermal neutron capture cross sections, *Phys. Rev.* 83 (3) (1951) 641–645.
- [65] S.D. Kaloshkin, V.V. Tcherdyntsev, M.V. Gorshenkov, V.N. Gulbin, S.A. Kuznetsov, Radiation-protective polymer-matrix nano structured composites, *J. Alloys Compd.* 536S (2012) S522–S526.
- [66] L. Liu, Y. Sheng, M. Liu, M. Dienwiebel, Z. Zhang, D. Daetan, Formation of the third bodies of steel sliding against brass under lubricated conditions, *Tribol. Int.* 140 (2019) 105727.
- [67] G.L. Tan, D. Tang, D. Dastan, A. Jafari, J.P.B. Silva, X.T. Yin, Effect of heat treatment on electrical and surface properties of tungsten oxide thin films grown by HFCVD technique, *Mater. Sci. Semicond. Process.* 122 (2021) 105506.